

Wigner solids of domain wall skyrmions

Kaifeng Yang¹, Katsumi Nagase², Yoshiro Hirayama^{2,3}, Tetsuya D. Mishima⁴, Michael B. Santos⁴ & Hongwu Liu^{1*}

¹State Key Lab of Superhard Materials, College of Physics, Jilin University, Changchun 130012, P. R. China.

²Department of Physics, Tohoku University, Sendai, Miyagi 980-8578, Japan.

³Center for Science and Innovation in Spintronics (Core Research Cluster), Tohoku University, Sendai, Miyagi 980-8577, Japan.

⁴Homer L. Dodge Department of Physics and Astronomy, University of Oklahoma, 440 West Brooks, Norman, OK 73019-2061, USA.

*email: hwliu@jlu.edu.cn

Abstract

Detection and characterization of a different type of topological excitations, namely the domain wall (DW) skyrmion, has received increasing attention because the DW is ubiquitous from condensed matter to particle physics and cosmology. Here we present experimental evidence for the DW skyrmion as the ground state stabilized by long-range Coulomb interactions in a quantum Hall ferromagnet. We develop an alternative approach using nonlocal resistance measurements together with a local NMR probe to measure the effect of low-current-induced dynamic nuclear polarization and thus to characterize the DW under equilibrium conditions. The dependence of nuclear spin relaxation in the DW on temperature, filling factor, quasiparticle localization, and effective magnetic fields allows us to interpret this ground state and its possible phase transitions in terms of Wigner solids of the DW skyrmion. These results demonstrate the importance of studying the intrinsic properties of quantum states that has been largely overlooked.

Introduction

The skyrmion, a topological soliton solution for the description of hadrons in 1960s¹, has attracted renewed interest in recent years due to its potential applications in information and communication technology demonstrated in magnetic materials^{2,3}. The magnetic skyrmion is classified by a topological charge $Q = \frac{1}{4\pi} \int \mathbf{n} \cdot (\partial_x \mathbf{n} \times \partial_y \mathbf{n}) dx dy$ counting the number of times that a unit vector \mathbf{n} of the local spin wraps around the unit sphere in a spherically symmetric or combed hedgehog configuration. The symmetric hedgehog skyrmion has also been found in an isotropic (fully spin-polarized) quantum Hall ferromagnet (QHF) at filling factor $\nu = 1$ of a two-dimensional electron gas (2DEG) in GaAs (called QH skyrmions)^{4,5}: it is energetically cheaper to constitute this spin texture than to have single spin flips for the GaAs 2DEG with sufficiently low bare Zeeman energy determined by a small effective g factor of -0.44. There is an alternative possibility for the realization of skyrmions once low-lying excited states of the domain wall (DW) as a one-dimensional (1D) object have nontrivial topological charge (referred to as DW skyrmions)⁶⁻⁹: the xy (z) component of a unit vector of spins gains a 2π (π) phase within the length (width) of this excitation along (across) the DW, defining a mapping topologically equivalent to the combed hedgehog sphere. The ubiquitous nature of the DW may hold promise for the creation and application of skyrmions in nonrelativistic and relativistic systems, which is of considerable importance from both theoretical and practical points of view.

More recently, the DW skyrmion has been demonstrated in chiral magnets with a strong Dzyaloshinskii-Moriya interaction induced by the spin-orbit coupling (SOC)¹⁰⁻¹². Unlike the magnetic skyrmion that can form a lattice as the ground state, the magnetic DW skyrmion is shown to be low-lying spin excitations. In this study, we present data demonstrating the ground state of DW skyrmions in an Ising (easy-axis) QHF (IQHF). In contrast to the magnetic DW skyrmion, the DW skyrmion in the IQHF is expected to carry an electrical charge due to the identity between topological and electrical

charge densities and to dominate the electronic properties of the IQHF as similar to the QH skyrmion^{6,13}. Therefore, we combine nonlocal resistance measurements with a resistively detected NMR (RDNMR) technique (hereafter called NRDNMR) as a highly sensitive and minimally invasive approach to determine the DW skyrmion in the simplest IQHF at $\nu = 2$ of an InSb 2DEG^{14,15}. The nuclear spin relaxation (NSR) measurement, a generally accepted methodology for determining the low-frequency spin textures in the QH system (e.g., QH skyrmions)¹⁶, shows an increase in magnetic fluctuations in the DW coupling to the nuclei with decreasing temperature and increasing localization. This strongly suggests that the DW skyrmion may condense into a 1D Wigner crystal stabilized by long-range Coulomb repulsions, which displays both continuous and discontinuous phase transitions depending on the way that the effective magnetic field¹⁷ between two approaching Landau levels (LLs) with opposite spins changes.

Results and discussion

Nonlocal resistance measurements. The nonlocal resistance measurement (see Methods and Supplementary Note 1) is known to play a unique role in the study of edge or surface states^{18,19}. In this work, we demonstrate that the nonlocal measurement can be used to determine the intrinsic properties of bulk states. The bulk state under study here is the $\nu = 2$ IQHF that is formed when the tilt angle θ (Fig. 1a) is tuned to bring the pseudospin-down $[(n, \sigma) = (0, \downarrow)]$ (where n and σ are the orbital and spin indices, respectively) and pseudospin-up $(1, \uparrow)$ LLs into degeneracy (Fig. 1b). It is shown in Fig. 1c that a resistance spike in longitudinal resistance $R_{SD,12}$ occurs between two separate LL peaks (one locates at ~ 11 T and the other above the maximum field of 15 T in our measurements), signaling the presence of the IQHF^{20,21}. Note that, for a simple level crossing, the two approaching LL peaks will merge into one¹⁴.

The IQHF was also identified by the RDNMR measurement of the Knight shift at $\nu = 2$ ¹⁵ and by the calculation based on the Hartree-Fock theory (see below). Large Zeeman and cyclotron splittings²² effectively decouple the edge and bulk channels in the InSb 2DEG with relatively low mobility, making it possible to perform the nonlocal measurement. Although the $\nu = 2$ IQHF is known to originate from dissipative transport through the DW channels^{6,21}, its nonlocal transport properties have not been described yet. Figure 1c shows that the resistance of this IQHF consists of fine structures (FSs) in the nonlocal measurement, in contrast to that (R_{LL}) of the LL peak outside the IQHF region. The FSs of two nonlocal configurations $R_{23,14}$ and $R_{14,23}$ are found to be different, however, they obey the reciprocity theorem $R_{kl,mn}^{+B} = R_{mn,kl}^{-B}$ (Supplementary Fig. 3) derived from the Onsager relation²³. Furthermore, the response of all FSs to temperature (T) is monotonic and in the opposite direction to that of R_{LL} (Fig. 1d). The T dependence of the FSs is dominated by the variable range hopping (VRH) mechanism (Supplementary Fig. 4) as similar to that of the spike²², while the decrease in R_{LL} at high temperatures originates from the phonon-assisted inter-edge-bulk scattering²⁴. From the VRH formula the B dependence of localization length ξ of the $\nu = 2$ IQHF for different measurement configurations is plotted in Fig. 1e. Note that the edge states corresponding to the two intersecting LLs become part of an array of the (bulk) domains in the $\nu = 2$ IQHF¹⁵, and in this case the current is mainly carried by the edge channel related to the lowest LL with negligible scattering to the bulk state. Therefore, the FSs are believed to be determined by the bulk properties of the IQHF. Moreover, these FSs are different from nonlocal resistance fluctuations observed in the LL peak of quantum wires that are induced by the resonant tunneling between edge states through the bulk localized state²⁵. Based on the bulk-edge model with independent edge- and bulk-components (see Ref. 18 and Supplementary Notes 1 & 2), the four-terminal resistance is only parametrized by the longitudinal resistance of the bulk state and in this sense all these resistances (e.g., $R_{23,14}$, $R_{14,23}$, and $R_{SD,12}$) are essentially identical. However, the bulk current I_i^N

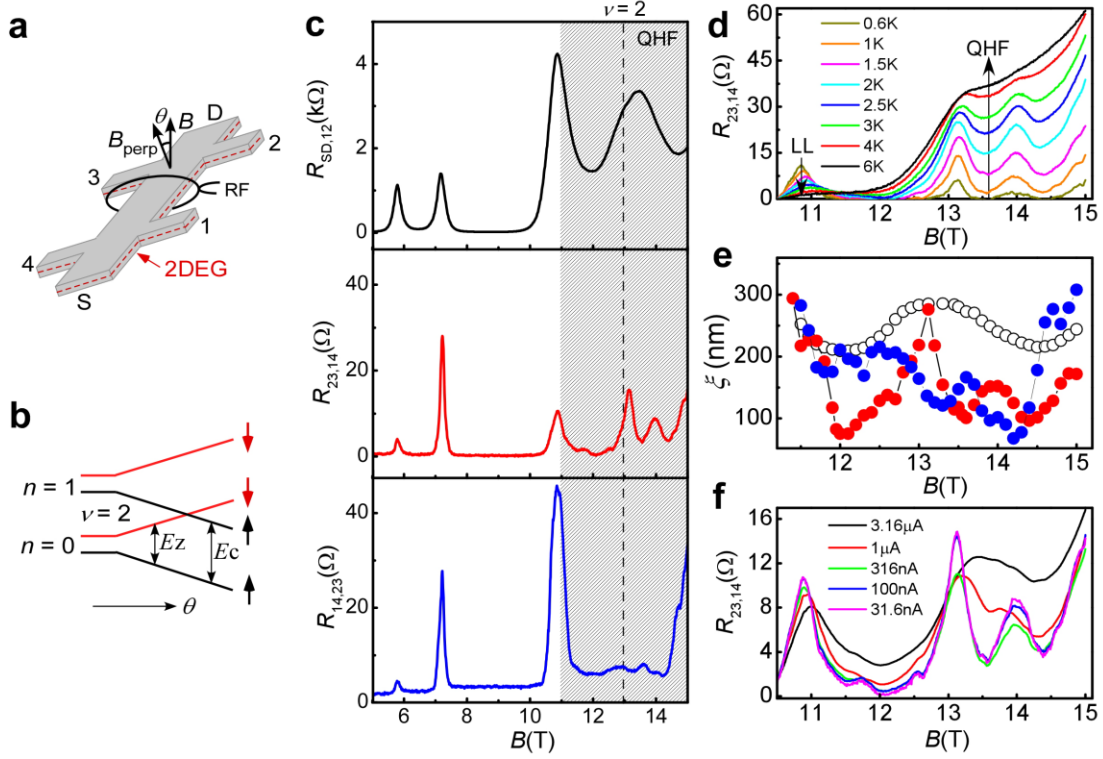


Figure 1. **Nonlocal resistance measurements of the Ising quantum Hall ferromagnet (IQHF) at filling factor $\nu = 2$.** **a** Schematics of a two-dimensional electron gas (2DEG, dashed line) Hall bar with six terminals (1-4, S, and D) surrounded by a coil that produces a continuous-wave radiofrequency (RF) field. The tilt angle θ is defined between the magnetic field B and its perpendicular component B_{perp} . **b** Schematics of the Landau level (LL) splitting as a function of θ . The $\nu = 2$ IQHF occurs when the two LLs with orbital index $n = 0$ and $n = 1$ intersects, where the Zeeman splitting $E_Z \sim B_{\text{perp}}/\cos\theta$ and the cyclotron gap $E_c \sim B_{\text{perp}}$ are made equal by adjusting θ . An upward (downward) arrow is for spin-up (spin-down). **c** Four-terminal resistance $R_{kl,mn}$ versus B at $T = 1\text{K}$, $I_{kl} = 31.6\text{ nA}$, and $\theta = 64^\circ$. The longitudinal resistance $R_{SD,12}$ is given by the ratio of a voltage drop V_{12} between terminals 1 and 2 to current flow I_{SD} between terminals S and D, and the nonlocal resistance $R_{23,14}$ ($R_{14,23}$) is calculated by V_{14}/I_{23} (V_{23}/I_{14}). Note the different scales for longitudinal and nonlocal resistances. The shaded area represents the $\nu = 2$ ($B \sim 13\text{T}$, dashed line) IQHF region. **d** $R_{23,14}$ versus B at different temperatures. The

arrow indicates increasing temperature. **e** Localization length ξ versus B obtained from a fit (Supplementary Fig. 4) to the B dependence of $R_{23,14}$ (red solid dots), $R_{14,23}$ (blue solid dots), and $R_{SD,12}$ (open dots) at different temperatures, respectively. **f** Current (I_{23}) dependence of $R_{23,14}$ versus B at $T = 1\text{K}$.

and the corresponding Hall electric field \mathcal{E}_H in each segment i depend on the measurement configurations, accounting for the difference between the spike and its nonlocal counterpart. The presence (absence) of the FSs in the B - ξ dependence of $R_{23,14}$ ($R_{SD,12}$) with $\mathcal{E}_H \sim 0.1 \text{ Vm}^{-1}$ ($\sim 14 \text{ Vm}^{-1}$) (see Supplementary Note 2) in Fig. 1e indicates an electric-field-dependent hopping transport; all FSs are broadened at large \mathcal{E}_H and thus merged into a single peak when the graded percolation problem is considered²⁶. This conclusion is further supported by the data in Fig. 1f, where the FSs for $R_{23,14}$ become a single peak as I_{23} increases up to $3.16 \mu\text{A}$ with $\mathcal{E}_H \sim 10 \text{ Vm}^{-1}$ and $I^N \sim 10 \text{ nA}$ (where I^N is the sum of I_i^N). In this case, the hopping transport is still in equilibrium (Supplementary Fig. 5), and the segments are electrically linear as evidenced by the fact that R_{LL} obeys the reciprocity theorem (Supplementary Fig. 6). However, the nonlocal resistance in the IQHF region does not satisfy the reciprocity theorem (Supplementary Fig. 6) because the Overhauser shift induced by dynamic nuclear polarization (DNP) breaks the Onsager relation locally. The effect of the DNP on nonlocal resistances was further investigated by the NRDNMR measurement (see Methods).

The NRDNMR signals of the $\nu = 2$ IQHF for $R_{23,14}^{\pm B}$ and $R_{14,23}^{\pm B}$ obtained at $I^N \sim 10 \text{ nA}$ and the RDNMR signals of the $\nu = 2$ IQHF for $R_{SD,12}$ at $I^N \sim 500 \text{ nA}$ are shown in Supplementary Figs. 8 and 9, respectively. Note that both RDNMR and NRDNMR signals are expected to be caused by the current-induced DNP^{14,27} responsible for the polarization of nuclei in the $\nu = 2/3$ QHF of GaAs 2DEGs, but the

underlying mechanism is still unclear^{15,16}. A shift of the $\nu = 2$ spike induced by the DNP with the degree of nuclear polarization of $\sim 10\%$ near the DW is assigned to cause the resistance change in the RDNMR measurement of the InSb 2DEG¹⁵. Relatively low nonlocal resistance (see Supplementary Note 2) responds more sensitively to subtle changes in the sample, thus accounting for the DNP performed by very low current in the NRDNMR measurement and for increased detection sensitivity: the maximum signal amplitude for $R_{23,14}^{\pm B}$ and $R_{14,23}^{\pm B}$ is ten times larger than that for $R_{SD,12}$. Furthermore, the NRDNMR signals for $R_{23,14}^{+B}$ and $R_{14,23}^{-B}$ are found to spread out over the $\nu = 2$ IQHF region but are sparsely distributed for $R_{23,14}^{-B}$ and $R_{14,23}^{+B}$. This suggests that the DW structure in which the DNP occurs depends on the measurement configurations, which is further supported by measurements of nuclear spin-lattice relaxation time T_1 and spin dephasing time T_2 (see Methods) as local probes of the low-frequency spin dynamics of the DW.

NRDNMR relaxation time measurements. We now discuss the T_1 and T_2 results of the $\nu = 2$ IQHF for $R_{14,23}^{+B}$. Figure 2a shows that T_1 near $\nu = 2$ is very short (~ 8 s) and gradually increases until $|2 - \nu| \sim 0.023$ (dashed line). Then T_1 increases sharply on the low (high)- ν side at 0.3 K (1 K) and decreases with decreasing ν (data on the high- ν side are not available). Details of the T -dependent T_1 are presented in Fig. 2b in terms of the nuclear spin-lattice relaxation rate $1/T_1$. It is clear that the dependence of $1/T_1$ on T is linear at $|2 - \nu| < 0.023$ (called phase I, Fig. 2a) but following an Arrhenius-like behavior at $|2 - \nu| > 0.023$ (phase II), demonstrating that different relaxation mechanisms are responsible for the two phases. Fast $1/T_1$ at $T \rightarrow 0$ in phase I is indicative of strong magnetic fluctuations coupling to the nuclei. Note that T_1 in the $\nu = 2$ IQHF obtained from the RDNMR measurement is independent of temperature as also observed in both the $\nu = 2/3$ QHF and the two-subband QHF of the GaAs 2DEG²⁸. All these results cannot be explained by a simple level crossing with single spin flips

taking account of disorder and electron exchange interaction that accounts for a slow NSR dominated by the Korringa law: $T_1 T = \text{const}^{28}$. Furthermore, $R_{14,23}^{+B}$ in phase I is found to be linear in T at large current for the NRDNMR measurement (inset, Fig. 2c), resulting in a linear dependence of $1/T_1$ on $R_{14,23}^{+B}$ (Fig. 2c). Because the localization of quasiparticles in the DW is expected to account for less conducting DWs, an increase in $1/T_1$ with decreasing $R_{14,23}^{+B}$ suggests that quasiparticle localization rather than additional conducting states dominates the NSR in the DW. This is opposite to the Korringa relaxation where $1/T_1$ is proportional to the resistance of the QH state²⁹. We point out that these findings are analogous to those of the $\nu \approx 1$ QH state in an extremely high-quality GaAs 2DEG as evidence for the formation of 2D skyrmion crystallization (SC)³⁰, a Wigner crystal with lattice points occupied by charged skyrmionic spin textures³¹. The DW in the QHF is expected to have electron spins noncollinear to B in the excited states including the spin wave (SW) and the DW skyrmion⁶. The thermally-activated transport measurement of both the $\nu = 2/3$ QHF and the two-subband QHF in the GaAs 2DEG suggests that low-lying excitations akin to the DW skyrmion may favor the NSR, but intricate composite-fermion interactions at $\nu = 2/3$ and the subband degree of freedom complicate the interpretation²⁸. Below we show that these excitations are necessarily related to the interpretation and discussion of our data.

The SOC in the IQHF treated as a perturbation due to its off-diagonal entries in the LL basis is expected to twist the planar (XY) component of \mathbf{n} with a 360° rotation along the DW, which lifts the degeneracy of the DW ground state and forms the DW skyrmion excitation⁶. The energy of the DW skyrmion is determined by the SOC strength in the form of $\alpha = \epsilon_{so}/\hbar\omega_c$ [see Ref. 6 and parameters given in Supplementary Table 1], in contrast to the case of QH skyrmions whose energy is determined by the effective g factor in the form of the Zeeman energy E_Z . Note that the QH skyrmion cannot be available in the InSb 2DEG where a relatively large g factor of $-39 \sim -88$ ³² makes the ratio of the Zeeman

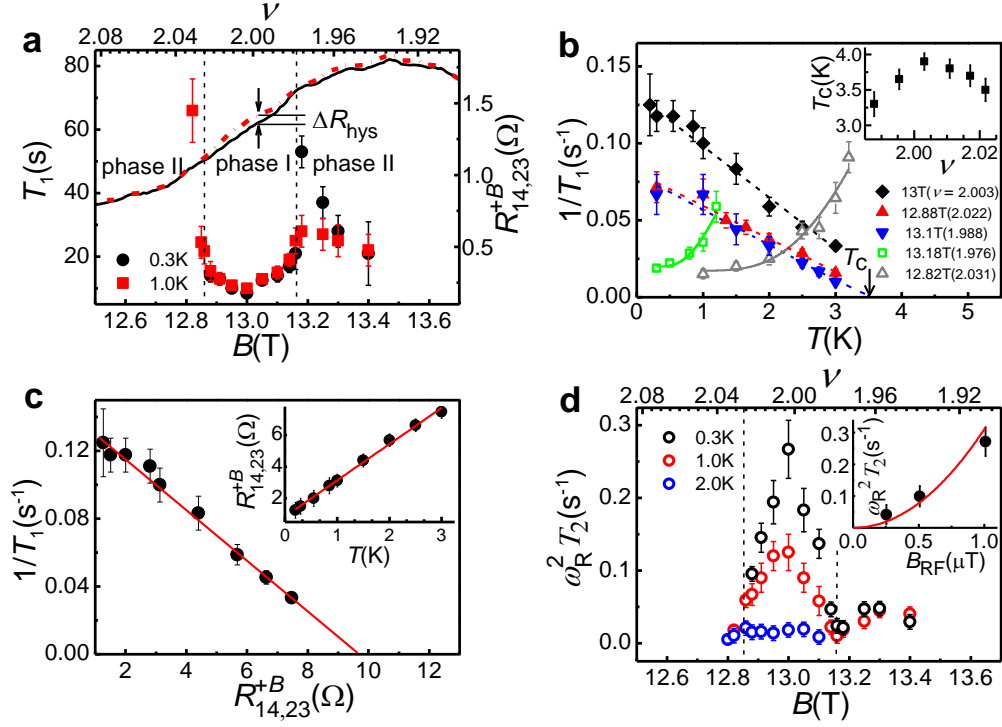


Figure 2. **Temperature and magnetic field dependence of T_1 and T_2 in the NRDNMR measurement of the Ising quantum Hall ferromagnet (IQHF) at $\nu = 2$.** **a** $R_{14,23}^{+B}$ (right y axis) as a function of B (or ν) swept upwards (solid line) and downwards (dash-dotted line) with a sweep rate of 1.7 mT/s at $I_{14} = 3.16 \mu\text{A}$, $\theta = 64^\circ$, and $T = 1 \text{ K}$. The B oriented parallel (opposite) to the normal direction of the 2DEG is written as $+(-)B$. ΔR_{hys} measures the magnitude of the resistance hysteresis at a fixed B . The NRDNMR signal occurs around $\nu = 2$ where the B (or ν) dependence of T_1 (left y axis) is obtained. The dashed line marks the phase boundary (see main text). Note that error bars for all data in this study are the standard deviation of the mean. **b** $1/T_1$ versus T at different B . The solid line is a fit to the data at 12.82 T (13.18 T) using the Arrhenius law with an activation energy Δ_{sw} of 1.36 (0.42) meV plus a T -independent constant of 0.02 s^{-1} . The dashed line is a linear fit, and its extrapolation to the x axis defines T_c at which $1/T_1$ is zero. Inset shows the ν dependence of T_c . **c** $1/T_1$ versus $R_{14,23}^{+B}$ obtained by comparing the T dependence of $R_{14,23}^{+B}$ at $B = 13 \text{ T}$ and $I_{14} = 3.16 \mu\text{A}$ (inset) and that of $1/T_1$ (data at $B = 13 \text{ T}$, Fig. 2b) point by point. The solid line is a guide to the eye. **d** $\omega_R^2 T_2$ versus B (or ν) at different temperatures.

The dashed line marks the phase boundary that is the same as that in **a**. The Rabi frequency $\omega_R = \gamma B_{\text{RF}}/2$ (where $\gamma = 9.36$ MHz/T is the gyromagnetic ratio of ^{115}In) is about 10 Hz (see Methods). Inset shows $\omega_R^2 T_2$ as a function of B_{RF} tuned by the RF output power. A good fit ($\propto B_{\text{RF}}^2$, solid line) to the data indicates a linear dependence of ω_R on B_{RF} .

and Coulomb energies 100 times larger than that required for its formation³³. It is shown in Supplementary Table 1 that α in the InSb 2DEG is only 3.8 times larger than that in the GaAs 2DEG while the difference in E_z between these two 2DEGs is significant (over 100 times). The DW skyrmion in the IQHF is able to carry electric charges as similar to the QH skyrmion¹³. The $\nu = 2$ IQHF occurs at zero effective field as discussed later, where dissipative transport in 1D DW channels percolating through the sample is responsible for $R_{14,23}^{+B}$. We expect that single DW skyrmions with long-range Coulomb repulsions will form a crystalline state in the 1D DW channels with quasi-long-range order analogous to the 1D Wigner crystal in carbon nanotubes^{34,35}, where a gapless XY spin wave mode with respect to the broken SO(2) symmetry would relax the nuclear spins more efficiently^{36,37} as shown by a short T_1 at $\nu = 2$ (Fig. 2a). Away from $\nu = 2$ a decrease in the number of DW skyrmions due to a nonzero $b^{*21,38}$ (positive for $\nu > 2$ and negative for $\nu < 2$, Supplementary Fig. 10) makes the crystal harder to form. A crystal of the DW skyrmion with low density is expected to melt at low temperatures because it is easier to break their bonds, as indicated in the inset of Fig. 2b where the state of phase I is found to be thermodynamically most stable up to ~ 4 K at $\nu = 2$. The NSR in less crystalline states is partially suppressed and therefore T_1 becomes longer. When moving further into the region of $|2 - \nu| > 0.023$ (phase II), a sudden change in T_1 signals a discontinuous transition to what we interpret as the SW-mediated NSR in neutral DWs with $Q = 0$. The Arrhenius-like behavior of $1/T_1$ in phase II (Fig. 2b)

indicates that the NSR occurs in low-energy excited states separated from the ground state by an energy gap Δ_{sw} . It is predicted that the neutral DW is preferably supported by a nonzero b^{*21} , where symmetry breaking induced by the SO interaction leads to the opening of a gap in the otherwise gapless spectrum of SW excitations^{6,39}. The number of neutral DWs increases with increasing $|b|$, resulting in a reduced Δ_{sw} by the SW-SW interaction⁴⁰ (Supplementary Fig. 11) that accounts for a drop in T_1 in phase II (Fig. 2a). Because of the difference in the NSR mode for phase I and phase II, the transformation between them is discontinuous that can be viewed as a first-order phase transition. This is responsible for a jump in T_1 between the two phases at low T (Fig. 2a). As T increases, the jump is smeared out (Fig. 2a) due to a decrease in T_1 in phase II caused by the Arrhenius behavior of thermal activation. Figure 2d shows the T and ν dependence of T_2 that is known to be dominated by dynamic fluctuating fields experienced by the nuclei in the quantum well associated with the dynamics of the 2DEG⁴¹. It is shown that T_2 in phase I decreases with increasing T in contrast to the motional narrowing effect, suggesting that the dynamics of the DW skyrmion is in the frozen limit where a very small number of free DW skyrmions suppresses the motion effect⁴². The 1D lattice of localized DW skyrmions may be responsible for the frozen limit that is taken as evidence for the localization of skyrmions in the 2D lattice⁴¹. In addition, T_2 drops off quickly with increasing $|2 - \nu|$ due to relatively strong nuclear dephasing in less crystalline states.

Figure 3a shows a contour plot of $\Delta R_{\text{hys}}/R_{14,23}^{+B}$ as a function of B and θ . The position of maximum $\Delta R_{\text{hys}}/R_{14,23}^{+B}$ is indicated by solid dots, where both $1/T_1$ and $\Delta R_{14,23}/R_{14,23}^{\text{sat}}$ are also at a maximum. The 1D DW channel percolating through the sample is expected to occur at these positions, in which more DW skyrmions are energetically favored. Based on many-body Hartree-Fock theory¹⁷, we have made a calculation of $b^* = 0$ in the B - B_{perp} plane (Supplementary Fig. 10) at which the IQHF occurs. It is seen that there is indeed an association between the theoretical $b^* = 0$ line and data points at these positions.

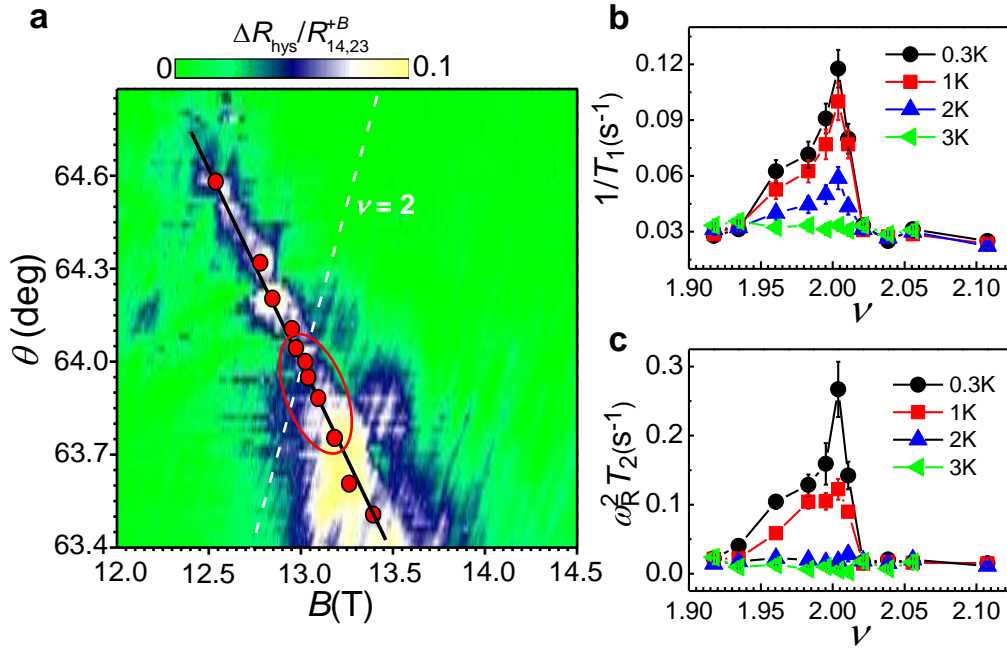


Figure 3. T_1 and T_2 results of the quantum Hall ferromagnet at $\nu = 2$ with zero effective field b^* . **a** Contour plot of B and θ dependence of $\Delta R_{\text{hys}}/R_{14,23}^{+B}$ at a field-sweep rate of 1.7 mT/s, $I_{14} = 3.16 \mu\text{A}$, and $T = 1$ K. Red dots indicate the position of maximum $\Delta R_{\text{hys}}/R_{14,23}^{+B}$, $1/T_1$, and $\Delta R_{14,23}/R_{14,23}^{\text{sat}}$. The solid line is a guide to the eye and the dashed line is calculated for the B and θ dependence of $\nu = 2$. Temperature dependence of $1/T_1$ (**b**) and $\omega_R^2 T_2$ (**c**) versus ν where the data (symbols) are in one-to-one correspondence with the red dots in (**a**) by $\nu = n_s h / e B \cos \theta$ (where h is Planck's constant and e the electron charge). It is clear that the data encircled by an oval in (**a**) exhibit a strong temperature dependence of T_1 and T_2 .

However, the position of these data points is different from that of maximum $R_{14,23}^{+B}$ (Supplementary Fig. 12) that is generally believed to be associated with $b^* = 0^{21}$. Our results demonstrate that the resistance measurement cannot establish this association in a straightforward manner. The T dependence of $1/T_1$

and T_2 at these positions in terms of ν is plotted in Fig. 3b, c. Note that these results were obtained along the $b^* = 0$ line rather than away from $b^* = 0$ (Fig. 2). Although the Wigner crystal of the DW skyrmion occurs at $\nu = 2$ with $b^* = 0$, it changes along the $b^* = 0$ line as shown by a nonmonotonic filling dependence of $1/T_1$ and T_2 with a peak around $\nu = 2$. This nonmonotonic behavior clearly rules out the possible role of exchange interactions at the Ising transition in $1/T_1$ and T_2 because the exchange-correlation energy varies monotonously along the $b^* = 0$ line²⁰. Away from $\nu = 2$ backscattering due to a finite density of extended states increases as indicated by an increase in resistance (Supplementary Fig. 13), which effectively induces random potential fluctuations to localize the eigenstates of the DW skyrmion and therefore makes the crystal harder to form. Although the T and ν dependence of $1/T_1$ and T_2 for these less crystalline states is similar to that in Fig. 2, the ν dependence is highly asymmetric because of the asymmetry of backscattering around $\nu = 2$ as indicated in Supplementary Fig. 13. Deep inside the strong backscattering region the DW skyrmions might have a clumped distribution between the potential wells behaving like a Wigner glass⁴³, which breaks the quasi-long-range order of the 1D Wigner crystal. The NSR in this region is probably caused by fluctuations of low-lying electronic states with energies smaller than $k_B T$ (where k_B is the Boltzmann constant), exhibiting the temperature-independent $1/T_1$ ⁴⁴. It is also seen that T_2 in the glassy regime is very short and temperature independent, indicating that more inhomogeneous local field fluctuations prevail over the motion effect for the nuclear dephasing. Note that the T_1 and T_2 properties of the glassy phase are the same as those of the $\nu = 2$ IQHF for other measurement configurations and also as those of the $\nu = 2$ IQHF obtained from the RDNMR measurement²⁸, suggesting that the presence of 1D Wigner glass of the DW skyrmion is responsible for the NSR therein. Furthermore, the T_1 property specified in the DW Wigner crystal and glass is qualitatively consistent with that predicted in the renormalized classical and quantum critical phases of

the skyrmion lattice^{45,46}, respectively, suggesting that the Wigner solid of the DW skyrmion is able to provide a rich test bed for experimental investigations and theoretical descriptions of quantum criticality.

Note that the width of the DW skyrmion is determined by the DW thickness of the order of magnetic length $l_B = 25.6 \text{ nm}/\sqrt{B\cos\theta}$ ($\sim 11 \text{ nm}$ at $\nu = 2$)¹⁵ and its length strongly depends on the SOC strength¹³. The formation of domain structure (several hundreds of nm in domain size¹⁵) in the InSb 2DEG with relatively low mobility does not allow the DW skyrmion to condense into the Wigner solid in 2D such as the 2D SC observed in a GaAs 2DEG with extremely high mobility³⁰. As discussed above, the electrons in the 1D DW channels percolating through the sample move in a correlated fashion, which is expected to dominate the dissipative transport and thus the NSR in the $\nu = 2$ IQHF. It should be pointed out that this 1D skyrmionic Wigner crystal cannot be obtained by laterally confining the 2D SC because of the confinement-induced melting effect⁴⁷. It is also impossible for the skyrmions in 1D nanowires⁴⁸ and for the magnetic DW skyrmions^{11,12} to condense into a Wigner solid due to the absence of the long-range nature of their interactions. The 1D Wigner crystal consisting of topological solitons instead of electrons is thermally stable up to $\sim 4 \text{ K}$ that will be further increased by optimizing the size of the DW skyrmions and thus their interactions, providing a platform where the Wigner crystal can be formed at high temperatures. We note that the 1D skyrmionic Wigner crystal discovered in this study is only distributed over a very narrow range of filling factors ($|2 - \nu| < 0.023$) in a certain measurement configuration with nonlocal resistance $R_{23,14}$ but quite robust to condition changes. Crucial to the success of this discovery is the development of the NRDNMR technique that makes it possible to construct and characterize the DW with different configurations under equilibrium conditions. Our results highlight the uniqueness of the NRDNMR technique in the determination of intrinsic properties of quantum states and of their phase transition. Results of the present study strongly suggest that attention should be paid

to previous transport and NMR measurements, where the role played by the Hall electric field has tended to be overlooked.

Methods

Nonlocal resistance measurement. The sample of 2DEGs in a 20-nm-wide InSb quantum well under study here was patterned into a Hall bar (100 μm length and 30 μm width) with Ti/Au as Ohmic contacts. A low-noise preamplifier (Stanford Research Systems, Model SR560) and an alternating current (AC) resistance bridge (Lake Shore Model 370) at 13.7 Hz were used for the direct current (DC) and AC measurements, respectively. It is shown in Supplementary Fig. 2 that the AC nonlocal resistance $R_{23,14}$ of the $\nu = 2$ IQHF and its DC counterpart $R_{23,14}^{\text{DC}+}$ ($R_{23,14}^{\text{DC}-}$) for positive (negative) current satisfy $R_{23,14} \approx \frac{1}{2}(R_{23,14}^{\text{DC}+} + R_{23,14}^{\text{DC}-})$, suggesting that the FSs are independent of the type of electric current. Because the signal-to-noise ratio of the DC NRDNMR measurement is relatively low, all other data shown in this manuscript were collected using the AC resistance bridge in a dilution refrigerator with in situ rotator stage. Low-temperature electron density of $n_s \sim 2.76 \times 10^{15} \text{ m}^{-2}$ and mobility of $\mu \sim 19.3 \text{ m}^2/\text{Vs}$ of the InSb 2DEG were obtained from the fast Fourier transform (FFT) analysis of low-field Shubnikov-de-Haas (SdH) oscillations and from the value of $R_{\text{SD},12}$ at $B = 0$, respectively.

NRDNMR, T_1 and T_2 measurements. The details of the NRDNMR measurement are shown in Supplementary Fig. 7: a relatively large current is applied to polarize the nuclei in the $\nu = 2$ IQHF region, as indicated by an exponential increase in the nonlocal resistance (for example, $R_{14,23}$) on a time scale of hundreds of seconds. After $R_{14,23}$ becomes saturated, a continuous-wave RF field at a resonance (Larmor) frequency of $f_{\text{NMR}} = \gamma B$ is applied to irradiate the 2DEG (on resonance). The RF field is generated by a single coil with 2 turns (a cross-sectional area of 3 mm \times 8 mm and a length of 4 mm) surrounding the sample connected to the RF generator using a 50 Ω coax cable. The change in $R_{14,23}$ representing the depolarization of nuclei reaches a maximum ΔR_{nl} at complete saturation ($R_{\text{nl}}^{\text{sat}}$) with the rise time $T_r =$

$T_1/(1 + \omega_R^2 T_1 T_2)$, where ω_R is the Rabi frequency. The component of the RF field perpendicular to B (B_{RF}) is estimated to be $\sim 2.2 \mu\text{T}$ for an RF output power of 0 dbm at $\theta = 64^\circ$ that gives $\omega_R \sim 10 \text{ Hz}$. As the RF frequency is detuned from f_{NMR} (off resonance), $R_{14,23}$ is decreased exponentially due to the repolarization of nuclei. The fall time of repolarization gives T_1 and thus T_2 is obtained from T_1 .

Data availability

The authors declare that data supporting the findings of this study are available within the paper and its supplementary information files.

References

1. Skyrme, T. H. R. A unified field theory of mesons and baryons. *Nucl. Phys.* **31**, 556-569 (1962).
2. Nagaosa, N. & Tokura, Y. Topological properties and dynamics of magnetic skyrmions. *Nature Nanotech.* **8**, 899-911 (2013).
3. Fert, A., Reyren, N. & Cros, V. Magnetic skyrmions: advances in physics and potential applications. *Nat. Rev. Mater.* **2**, 17031 (2017).
4. Sondhi, S. L., Karlhede, A., Kivelson, S. A. & Rezayi, E. H. Skyrmions and the crossover from the integer to fractional quantum Hall effect at small Zeeman energies. *Phys. Rev. B* **47**, 16419-16426 (1993).
5. Barrett, S. E., Dabbagh, G., Pfeiffer, L. N., West, K. W. & Tycko, R. Optically pumped NMR evidence for finite-size skyrmions in GaAs quantum wells near Landau level filling $\nu = 1$. *Phys. Rev. Lett.* **74**, 5112-5115 (1995).
6. Fal'ko, V. I. & Iordanskii, S. V. Topological defects and Goldstone excitations in domain walls between ferromagnetic quantum Hall liquids. *Phys. Rev. Lett.* **82**, 402-405 (1999).
7. Nitta, M. Matryoshka Skyrmions. *Nucl. Phys. B* **872**, 62-71 (2013).
8. Jennings, P. & Sutcliffe, P. The dynamics of domain wall Skyrmions. *J. Phys. A: Math. Theor.* **46**, 465401 (2013).
9. Danon, J., Balram, A. C., Sánchez, S. & Rudner, M. S. Charge and spin textures of Ising quantum Hall ferromagnet domain walls. *Phys. Rev. B* **100**, 235406 (2019).
10. Cheng, R., Li, M., Sapkota, A., Rai, A., Pokhrel, A., Mewes, T., Mewes, C., Xiao, D., De Graef, M. & Sokalski, V. Magnetic domain wall skyrmions. *Phys. Rev. B* **99**, 184412 (2019).

11. Li, M., Sapkota, A., Rai, A., Pokhrel, A., Mewes, T., Mewes, C., Xiao, D., De Graef, M. & Sokalski, V. Magnetic domain wall structures in Pt/Co/Ni/Ir multi-layers. Preprint at <https://arXiv.org/abs/2004.07888> (2020).
12. Nagase, T., So, Y. G., Yasui, H., Ishida, T., Yoshida, H. K., Tanaka, Y., Saito, K., Ikarashi, N., Kawaguchi, Y., Kuwahara, M. & Nagao, M. Observation of domain wall bimerons in chiral magnets. *Nat. Commun.* **12**, 3490 (2021).
13. Brey, L. & Tejedor, C. Spins, charges, and currents at domain walls in a quantum Hall Ising ferromagnet. *Phys. Rev. B* **66**, 041308(R) (2002).
14. Liu, H. W., Yang, K. F., Mishima, T. D., Santos, M. B. & Hirayama, Y. Dynamic nuclear polarization and nuclear magnetic resonance in the simplest pseudospin quantum Hall ferromagnet. *Phys. Rev. B* **82**, 241304(R) (2010).
15. Yang, K. F., Nagase, K., Hirayama, Y., Mishima, T. D., Santos, M. B. & Liu, H. W. Role of chiral quantum Hall edge states in nuclear spin polarization. *Nat. Commun.* **8**, 15084 (2017).
16. Hirayama, Y., Yusa, G., Hashimoto, K., Kumada, N., Ota, T. & Muraki, K. Electron-spin/nuclear-spin interactions and NMR in semiconductors. *Semicond. Sci. Technol.* **24**, 023001 (2009).
17. Jungwirth, T. & MacDonald, A. H. Pseudospin anisotropy classification of quantum Hall ferromagnets. *Phys. Rev. B* **63**, 035305 (2000).
18. McEuen, P. L., Szafer, A., Richter, C. A., Alphenaar, B. W., Jain, J. K., Stone, A. D., Wheeler, R. G. & Sacks, R. N. New resistivity for high-mobility quantum Hall conductors. *Phys. Rev. Lett.* **64**, 2062-2065 (1990).

19. Abanin, D. A., Morozov, S. V., Ponomarenko, L. A., Gorbachev, R. V., Mayorov, A. S., Katsnelson, M. I., Watanabe, K., Taniguchi, T., Novoselov, K. S., Levitov, L. S. & Geim, A. K. Giant nonlocality near the Dirac point in graphene. *Science* **332**, 328-330 (2011).
20. De Poortere, E. P., Tutuc, E., Papadakis, S. J. & Shayegan, M. Resistance spikes at transitions between quantum Hall ferromagnets. *Science* **290**, 1546-1549 (2000).
21. Jungwirth, T. & MacDonald, A. H. Resistance spikes and domain wall loops in Ising quantum Hall ferromagnets. *Phys. Rev. Lett.* **87**, 216801 (2001).
22. Yang, K. F., Liu, H. W., Nagase, K., Mishima, T. D., Santos, M. B. & Hirayama, Y. Resistively detected nuclear magnetic resonance via a single InSb two-dimensional electron gas at high temperature. *Appl. Phys. Lett.* **98**, 142109 (2011).
23. Büttiker, M. Four-terminal phase-coherent conductance. *Phys. Rev. Lett.* **57**, 1761-1764 (1986).
24. Wang, J. K. & Goldman, V. J. Measurements and modeling of nonlocal resistance in the fractional quantum Hall effect. *Phys. Rev. B* **45**, 13479-13487 (1992).
25. Main, P. C., Geim, A. K., Carmona, H. A., Brown, C. V., Foster, T. J., Taboryski, R. & Lindelof, P. E. Resistance fluctuations in the quantum Hall regime. *Phys. Rev. B* **50**, 4450-4455 (1994).
26. Trugman, S. A. Localization, percolation, and the quantum Hall effect. *Phys. Rev. B* **27**, 7539-7546 (1983).
27. Korkusinski, M., Hawrylak, P., Liu, H. W. & Hirayama, Y. Manipulation of a nuclear spin by a magnetic domain wall in a quantum Hall ferromagnet. *Sci. Rep.* **7**, 43553 (2017).

28. Yang, K. F., Uddin, M. M., Nagase, K., Mishima, T. D., Santos, M. B., Hirayama, Y., Yang, Z. N. & Liu, H. W. Pump-probe nuclear spin relaxation study of the quantum Hall ferromagnet at filling factor $\nu = 2$. *New J. Phys.* **21**, 083004 (2019)
29. Desrat, W., Maude, D. K., Potemski, M., Portal, J. C., Wasilewski, Z. R. & Hill, G. Resistively detected nuclear resonance in the quantum Hall regime: Possible evidence for a Skyrme crystal. *Phys. Rev. Lett.* **88**, 256807 (2002).
30. Gervais, G., Stormer, H. L., Tsui, D. C., Kuhns, P. L., Moulton, W. G., Reyes, A. P., Pfeiffer, L. N., Baldwin, K. W. & West, K. W. Evidence for skyrmions crystallization from NMR relaxation experiments. *Phys. Rev. Lett.* **94**, 196803 (2005).
31. Zhu, H., Sambandamurthy, G., Chen, Y. P., Jiang, P., Engel, L. W., Tsui, D. C., Pfeiffer, L. N. & West, K. W. Pinning-mode resonance of a Skyrme crystal near Landau-level filling factor $\nu = 1$. *Phys. Rev. Lett.* **104**, 226801 (2010).
32. Yang, K. F., Liu, H. W., Mishima, T. D., Santos, M. B., Nagase, K. & Hirayama, Y. Nonlinear magnetic field dependence of spin polarization in high-density two-dimensional electron systems. *New J. Phys.* **13**, 083010 (2011).
33. Fertig, H. A., Brey, L., Côté, R. & MacDonald, A. H., Charged spin-texture excitations and the Hartree-Fock approximation in the quantum Hall effect. *Phys. Rev. B* **50**, 11018-11021 (1994).
34. Schulz, H. J. Wigner crystal in one dimension. *Phys. Rev. Lett.* **71**, 1864-1867 (1993).
35. Shapir, I., Hamo, A., Pecker, S., Moca, C. P., Legeza, Ö., Zarand G. & Ilani, S. Imaging the electronics Wigner crystal in one dimension. *Science* **364**, 870-875 (2019).
36. Côté, R., MacDonald, A. H., Brey, L., Fertig, H. A., Girvin, S. M. & Stool, H. T. C. Collective excitations, NMR, and phase transitions in Skyrme crystals. *Phys. Rev. Lett.* **78**, 4825-4828 (1997).

37. Fertig, H. A. & Brey, L. Luttinger liquid at the edge of undoped graphene in a strong magnetic field. *Phys. Rev. Lett.* **97**, 116805 (2006).
38. Fal'ko, V. I. & Iordanskii, S. V. Spin-orbit coupling effect on quantum Hall ferromagnets with vanishing Zeeman energy. *Phys. Rev. Lett.* **84**, 127-130 (2000).
39. Mitra, A. & Girvin, S. M. Electron/nuclear spin domain walls in quantum Hall systems. *Phys. Rev. B* **67**, 245311 (2003).
40. Kasner, M., Palacios, J. J. & MacDonald, A. H. Quasiparticle properties of quantum Hall ferromagnets. *Phys. Rev. B* **62**, 2640-2658 (2000).
41. Khandelwal, P., Dementyev, A. E., Kuzma, N. N., Barrett, S. E., Pfeiffer, L. N. & West, K. W. Spectroscopic evidence for the localization of skyrmions near $\nu = 1$ as $T \rightarrow 0$. *Phys. Rev. Lett.* **86**, 5353-5356 (2001).
42. Villares Ferrer, A., Doretto, R. L. & Caldeira, A. O. NMR linewidth and skyrmion localization in quantum Hall ferromagnets. *Phys. Rev. B* **70**, 045319 (2004).
43. Akhanjee, S. & Rudnick, J. Disorder induced transition into a one-dimensional Wigner glass. *Phys. Rev. Lett.* **99**, 236403 (2007).
44. Tycko, R., Barrett, S. E., Dabagh, G., Pfeiffer, L. N. & West, K. W. Electronic states in gallium arsenide quantum wells probed by optically pumped NMR. *Science* **268**, 1460-1463 (1995).
45. Read, N. & Sachdev, S. Continuum quantum ferromagnets at finite temperature and the quantum Hall effect. *Phys. Rev. Lett.* **75**, 3509-3512 (1995).
46. Green, A. G. Quantum-critical dynamics of the Skyrmion lattice. *Phys. Rev. B* **61**, R16299-R16302 (2000).

47. Kobayashi, T., Kumada, N., Ota, T., Sasaki, S. & Hirayama, Y. Low-frequency spin fluctuations in skyrmions confined by wires: Measurement of local nuclear spin relaxation. *Phys. Rev. Lett.* **107**, 126807 (2011).
48. Lin, S. Z., Reichhardt, C., Batista, C. D. & Saxena, A. Particle model for skyrmions in metallic chiral magnets: Dynamics, pinning, and creep. *Phys. Rev. B* **87**, 214419 (2013).

Acknowledgments

We thank G. Yusa, K. Muraki, and N. Kumada for helpful discussions. This work was supported by the National Natural Science Foundation of China (11974132 and 11704144), the Jilin Natural Science Foundation (20180101286JC), the Fundamental Research Funds for the Central Universities, the JST-ERATO, the KAKENHI (15H05867 and 18H01811), and the CSRN (Y.H.) and the GP-Spin (K.N. and Y.H.) in Tohoku University.

Author contributions

H.W.L. designed and supervised the research. K.F.Y. performed the experiments and collected the data. K.N. and Y.H. fabricated InSb/AlInSb Hall bars. T.D.M. and M.B.S. grew InSb heterostructures. H.W.L. and K.F.Y. analyzed the data. H.W.L. wrote the manuscript.

Competing interests

None of the authors have a competing interest.

Additional Information

Supplementary Information is available for this paper.

Correspondence and requests for materials should be addressed to H.W.L.

Supplementary Information for

Wigner solids of domain wall skyrmions

Kaifeng Yang, Katsumi Nagase, Yoshiro Hirayama, Tetsuya D. Mishima,

Michael B. Santos & Hongwu Liu*

*email: hwliu@jlu.edu.cn

The PDF file includes:

Supplementary Notes 1-3

Supplementary Figures 1-13

Supplementary Table 1

Supplementary References 1-8

Supplementary Note 1: Edge-channel model for the quantum Hall effect

It is modeled by an edge-channel picture of the quantum Hall effect (Supplementary Fig. 1) to specify sufficient conditions for the appearance of nonlocal resistances¹. The difference in electrochemical potentials between two terminals is given by $\mu_2 - \mu_1 \approx t_2(1 - t_1)(\mu_B - \mu_E)/(N - 1)$, where μ_B and μ_E are fictitious chemical potentials for the $N-1$ edges with perfect transmission through the barrier and the N th (bulk) channel with transmission probabilities t_1 and t_2 , respectively. Apparently, there exists a voltage when the edge and bulk channels are decoupled (i.e., $\mu_B \neq \mu_E$) and $t_{1(2)} \neq 1(0)$, no matter whether a net current flows between these two terminals or not and whether they are separated by a short or long distance. With the help of edge states that carry the current to classically inaccessible region, the nonlocal resistance thus occurs even when the voltage probes are separated from the current path over a macroscopic distance.

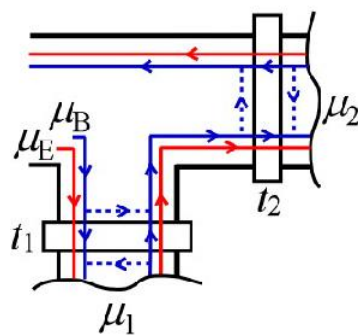
Supplementary Note 2: Estimation of bulk current and Hall electric fields in the quantum Hall ferromagnet at filling factor $\nu = 2$

The four-terminal resistance in the bulk-edge model of a quantum Hall conductor with independent edge- and bulk-current components is approximated by $R_{kl,mn} \propto I^N R / I_{kl}$ [where I^N is the sum of the bulk current carried by the highest occupied (N th) Landau level (LL) in the corresponding segments associated with measurement configurations]², assuming for simplicity that all segments have the same longitudinal resistance R and the current distribution near a contact is homogeneous. Note that the bulk current I_i^N in segment i of voltage probes characterized by the total current $I_i^t = 0$ is converted from the edge current. Because the edge current flowing into or out of the voltage probe is determined by the direction of B rather than by the polarity of the applied current, the difference between ingoing and outgoing edge currents on opposite sides of the voltage probe leads to a direct current (DC) I_i^N for a given direction of B . Therefore, a DC rather than an alternating current (AC) signal is obtained from the AC nonlocal measurement. The Hall electric field in the bulk state of the N th LL of segment i is $\mathcal{E}_H = \rho_{xy}^N I_i^N / W$ (where ρ_{xy}^N is the Hall resistivity of the N th LL and W is the segment width). I^N for the spike of $R_{SD,12}$ (Fig. 1c, main text) has a maximum value of 15.8 nA based on the assumption that the applied

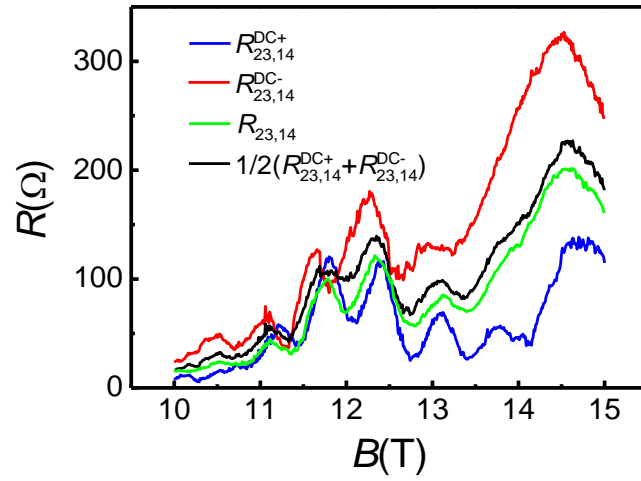
current $I_{SD} = 31.6$ nA is carried equally by the edge and bulk states. The value of this current corresponds to $\mathcal{E}_H \sim 14$ Vm⁻¹ calculated by $W = 30$ μm and by $\rho_{xy}^N = h/e^2$ (where h is Planck's constant) that is taken to be independent of the filling factor of the N th LL for simplicity. Comparison of $R_{23,14}$ and $R_{SD,12}$ around 13 T in Fig. 1c gives an estimate of an upper bound of $I^N \sim 0.1$ nA and $\mathcal{E}_H \sim 0.1$ Vm⁻¹ for the nonlocal counterpart of the spike according to $R_{kl,mn} \propto I^N R/I_{kl}$. Similarly, the current-independent $R_{23,14}$ around 13 T (Fig. 1f, main text) yields $I^N \sim 10$ nA and $\mathcal{E}_H \sim 10$ Vm⁻¹ for $I_{23} = 3.16$ μA. From the above discussion it is clear that a small value of I^N/I_{kl} results in relatively low nonlocal resistance that responds more sensitively to subtle change in the sample. This makes it possible to measure the effect of dynamic nuclear polarization (DNP) on the nonlocal resistance at low current accompanied by a small Hall electric field in the bulk, thus allowing for the NRDNMR measurement of the DW structure under equilibrium conditions that is not available by conventional methods.

Supplementary Note 3: Calculation of the effective magnetic field b^*

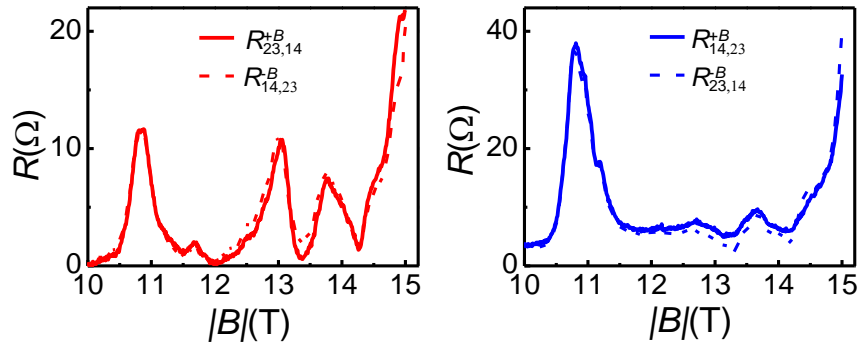
The effective field b^* measures the energy separation between the two approaching LLs with opposite spins (Fig. 1b, main text), including both single-particle LL splitting and interaction contributions^{3,4}. The b^* oriented along the z pseudospin direction near $\nu = 2$ is given by $b^* = b_z - U_{z,z}$. Here $b_z = -(E_z - E_c + I_0)/2$ (where E_z and E_c are the Zeeman and cyclotron energies, respectively) with the exchange interaction term $I_0 = 1/2 \sqrt{\pi/2} (e^2/4\pi\epsilon_0\epsilon l_B)$ (where e is the electron charge, ϵ_0 the vacuum permittivity, ϵ the dielectric constant and l_B the magnetic length) and $U_{z,z} = -1/8 \int_0^\infty dq e^{-q^2/2} \left[L_{n(\downarrow)}\left(\frac{q^2}{2}\right) - L_{m(\uparrow)}\left(\frac{q^2}{2}\right) \right]^2 (1 + e^{-dq})$ (where $L_{n,m}(x)$ is the Laguerre polynomial with $n = 0$ and $m = 1$ for $\nu = 2$ and d is the well thickness) is called the magnetic anisotropic term that depends on the nature of the intersected LLs.



Supplementary Figure 1. **Edge-channel schematics for the quantum Hall effect.** Model of multi-terminal conductors with each rectangular segment representing a barrier that perfectly transmits the $N-1$ edges (red line) but probably backscatters the N th channel (blue line) as shown by dashed lines, where N is the number of states at the Fermi level. The arrow indicates the direction of electron flow.

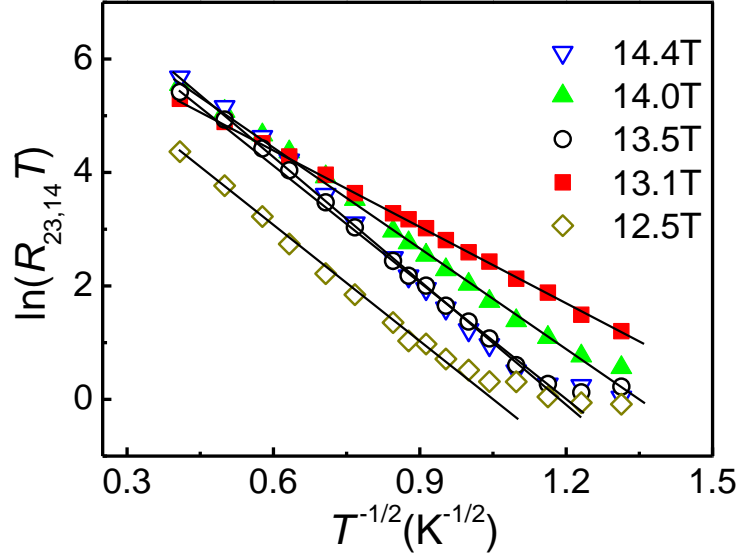


Supplementary Figure 2. **Nonlocal resistance of the quantum Hall ferromagnet at filling factor $\nu = 2$.** $R_{23,14}^{\text{DC}+}$ ($R_{23,14}^{\text{DC}-}$) for a positive (negative) direct current (DC) and $R_{23,14}$ for an alternating current (AC) as a function of the magnetic field B were measured in a JANIS cryostat at $T = 1.6$ K and $\vartheta = 64^\circ$.



Supplementary

Figure 3. **Nonlocal resistance under magnetic-field reversal for small currents.** $R_{23,14}^{\pm B}$ and $R_{14,23}^{\pm B}$ as a function of the absolute value of \mathbf{B} ($|B|$) at $I_{14(23)} = 31.6$ nA, $T = 1$ K, and $\vartheta = 64^\circ$.



Supplementary Figure 4. **Temperature dependence of the nonlocal resistance of the $\nu = 2$ quantum Hall ferromagnet (QHF) at different magnetic fields.** Data (symbols) are obtained from those in Fig.

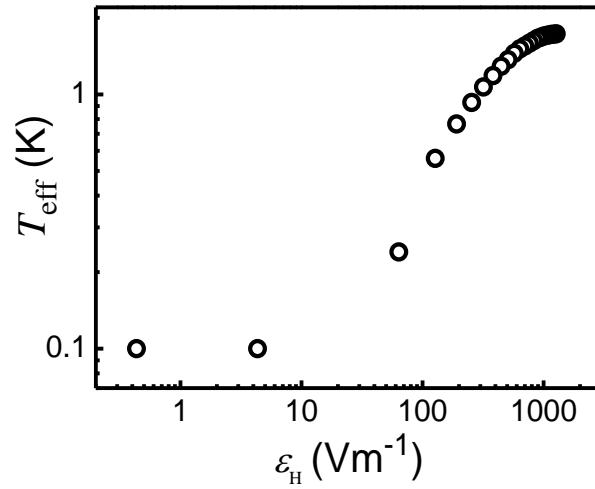
1d (see main text). The solid line is calculated by $R_{23,14} \propto \frac{1}{T} \exp\left[-\sqrt{\frac{T_0}{T}}\right]$, from which the localization

length $\xi = C \frac{e^2}{4\pi\epsilon_0 k_B T_0}$ (where k_B is the Boltzmann constant, e the electron charge, ϵ_0 the vacuum permittivity, dielectric constant $\epsilon = 16.8$, and $C \approx 6^5$) is derived (Fig. 1e, main text). Note that the

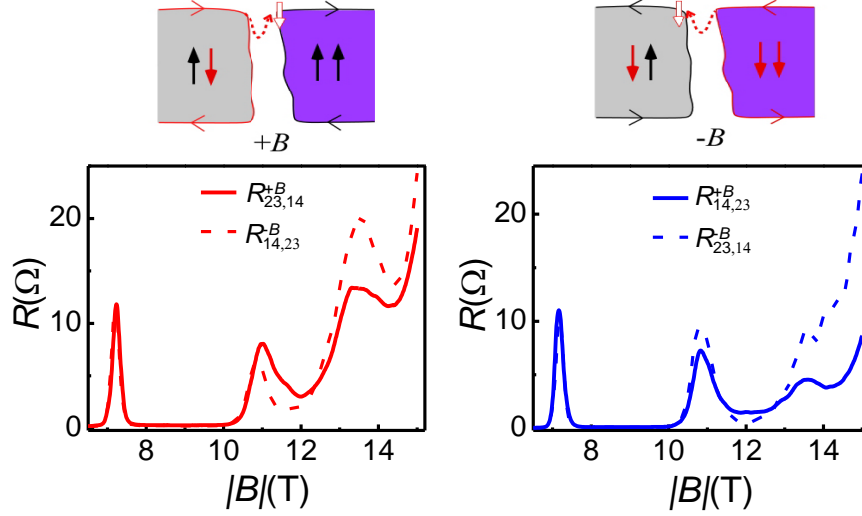
variable-range-hopping conductivity $\sigma_{xx}(T) \propto \frac{1}{T} \exp\left(-\sqrt{\frac{T_0}{T}}\right)$ is related to the longitudinal (Hall)

resistivity ρ_{xx}^N (ρ_{xy}^N) of the N th Landau level by $\sigma_{xx}^N = \rho_{xx}^N / [(\rho_{xx}^N)^2 + (\rho_{xy}^N)^2]$ with $\rho_{xy}^N \approx 26 \text{ k}\Omega$.

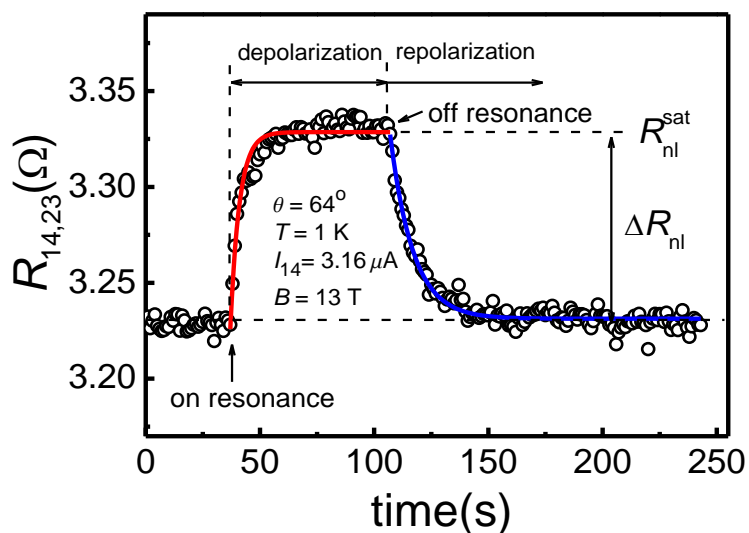
Because $R_{23,14} \propto I^N R / I_{23}$ and R is proportional to ρ_{xx}^N , $R_{23,14} \propto \rho_{xx}^N \propto \sigma_{xx}^N$ for $\rho_{xy}^N \gg \rho_{xx}^N$ in our case. That is, the bulk conduction of the $\nu = 2$ QHF changes with temperature in the same manner as the resistance.



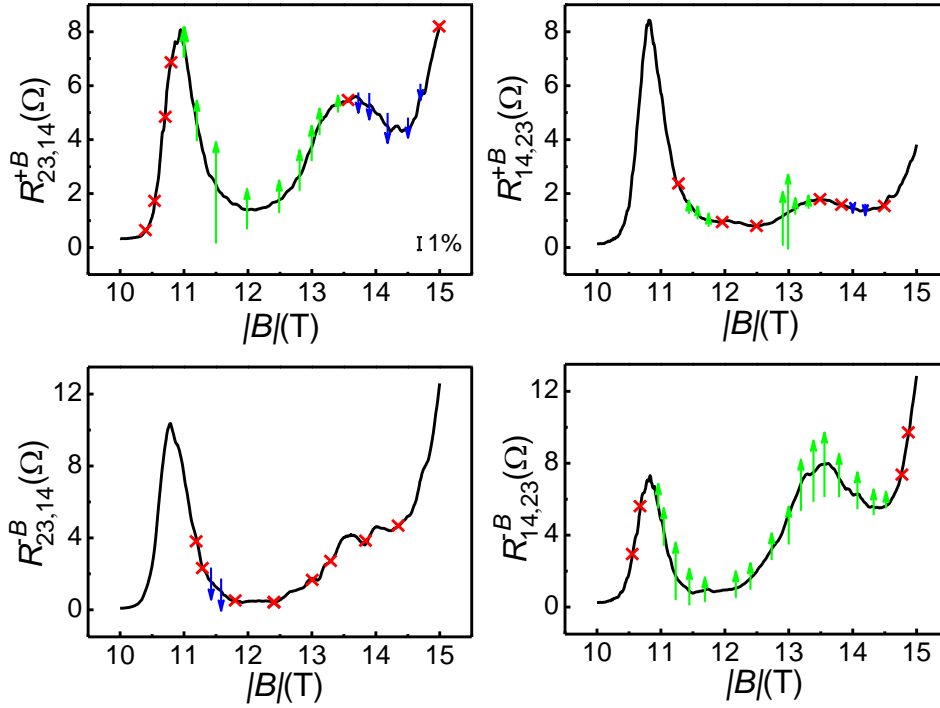
Supplementary Figure 5. **Hall-field-dependent variable range hopping transport.** Effective temperature T_{eff} versus the Hall electric field \mathcal{E}_H for $R_{23,14}$ in Fig. 1d (see main text) at $B = 13.5$ T and $T = 100$ mK. T_{eff} is obtained by comparing the measured $R_{\text{SD},12}(T) \equiv R_{\text{SD},12}(I_{\text{SD}})$ point by point, which is related to the existence of a quasi-Fermi level at large \mathcal{E}_H ⁶.



Supplementary Figure 6. **Nonlocal resistance under magnetic-field reversal for large currents.** $R_{23,14}^{\pm B}$ and $R_{14,23}^{\pm B}$ as a function of $|B|$ at $I_{14(23)} = 3.16 \mu\text{A}$, $T = 1 \text{ K}$ and $\vartheta = 64^\circ$. The panel depicts domain structures of the quantum Hall ferromagnet (QHF) formed at filling factor $\nu = 2$. The black (red) solid arrow denotes the spin-up (spin-down) electron. The gray and purple areas denote the spin-unpolarized and spin-polarized domains, respectively, and a domain (DW) occurs in between. A line surrounding each domain represents the edge state that becomes part of an array of domains. The nuclei (hollow arrow) polarized by the electron-spin flip (red dashed arrow) locate on either side of the DW, depending on the direction of edge current flow determined by the sign of the magnetic field B . The polarized nuclei will change static magnetic fields locally via the Overhauser effect, breaking the Onsager relation and thus the reciprocity theorem $R_{kl,mn}^{+B} = R_{mn,kl}^{-B}$ in the $\nu = 2$ ($|B| \sim 13 \text{ T}$) QHF region. In contrast, the nonlocal resistance of the Landau-level peak outside the QHF region ($|B| \sim 7.2 \text{ T}$) is found to obey the reciprocity theorem.



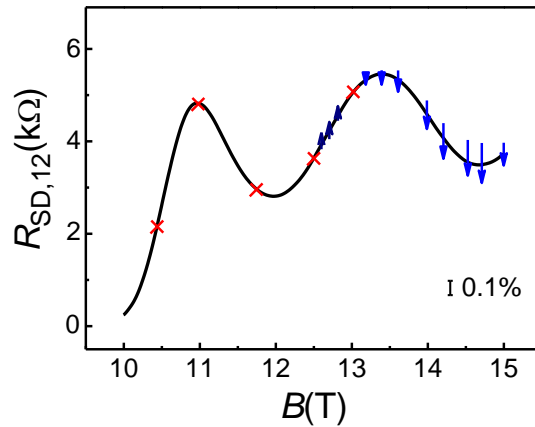
Supplementary Figure 7. **Time dependence of $R_{14,23}$ in the NRDNMR measurement.** The depolarization (repolarization) of nuclei under the condition of on (off) resonance with a continuous-wave radio-frequency matching (mismatching) the resonance frequency of ^{115}In is indicated by an exponential increase (decrease) of $R_{14,23}$. $R_{14,23}$ becomes saturated (R_{nl}^{sat}) at the end of depolarization, resulting in a resistance change ΔR_{nl} . The red (blue) line is an exponential fit to the data in the depolarization (repolarization) process, from which the nuclear spin-lattice relaxation time T_1 and the nuclear spin dephasing time T_2 are derived.



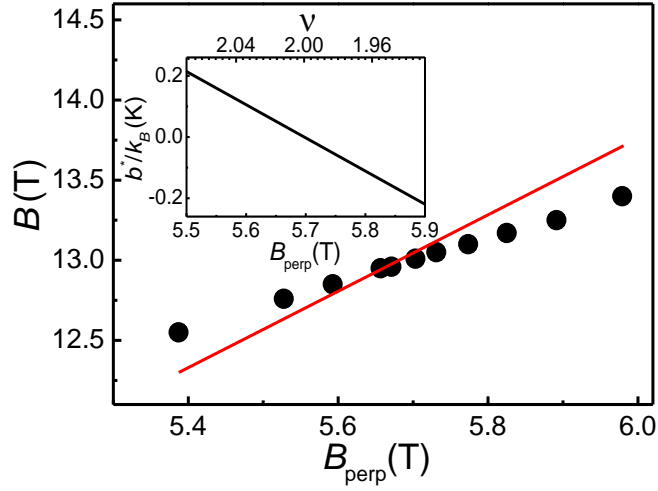
Supplementary Figure 8. **NRDNMR signals of the quantum Hall ferromagnet at filling factor $\nu = 2$.**

$R_{23,14}^{\pm B}$ and $R_{14,23}^{\pm B}$ as a function of the absolute value of B ($|B|$) at $I_{14(23)} = 3.16 \mu\text{A}$, $T = 1$ K, and $\vartheta = 64^\circ$.

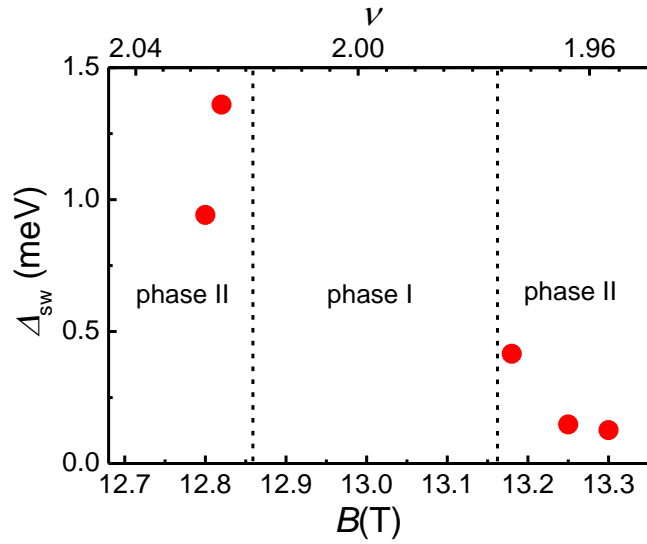
The amplitude and sign of $\Delta R_{\text{nl}}/R_{\text{nl}}^{\text{sat}}$ (Supplementary Fig. 7) are indicated by arrow length (scale bar, 1%) and direction, respectively. Note that the sign, as expected, depends on the relative shift of the nonlocal counterpart of the spike before and after the dynamic nuclear polarization. A cross (\times) indicates the absence of NRDNMR signals.



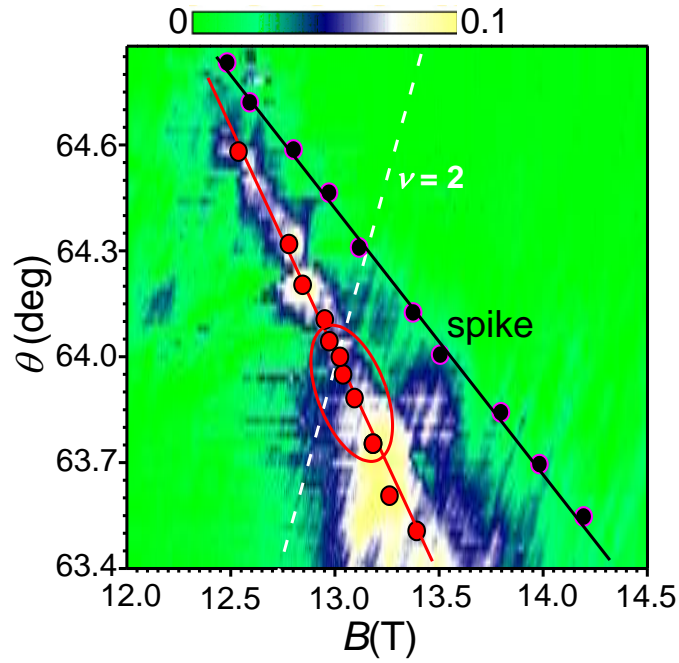
Supplementary Figure 9. **RDNMR signals of the quantum Hall ferromagnet at filling factor $\nu=2$.** $R_{SD,12}$ as a function of B at $I_{12} = 1 \mu\text{A}$ corresponding to $I^N \sim 500 \text{ nA}$ (see Supplementary Note 2), $T = 50 \text{ mK}$, and $\vartheta = 64^\circ$. The amplitude and sign of $\Delta R_{SD,12}/R_{SD,12}^{\text{sat}}$ induced by the dynamic nuclear polarization (DNP) are indicated by arrow length (scale bar, 0.1%) and direction, respectively. Note that the sign is expected to depend on the relative shift of the $\nu=2$ ($B \sim 13 \text{ T}$) spike before and after the DNP. A cross (\times) indicates the absence of RDNMR signals.



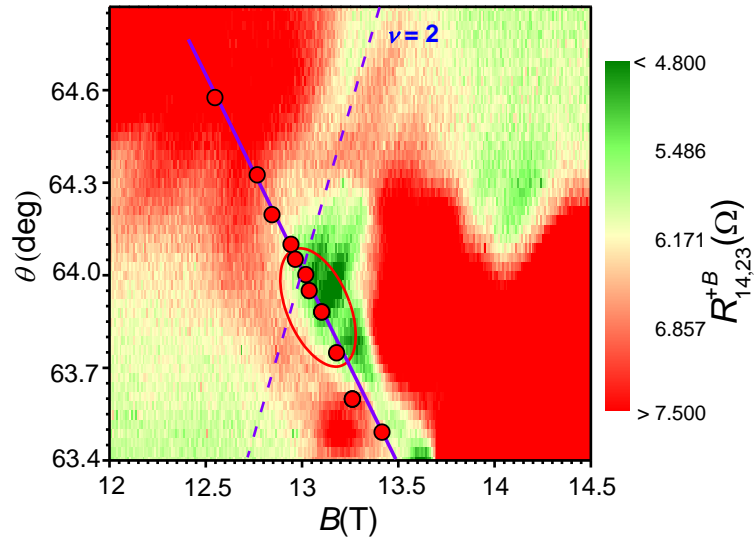
Supplementary Figure 10. **Zero effective field b^* in the (B, B_{perp}) plane.** Data (dots) in Fig. 2a (see main text) plotted as a function of the magnetic field B and its perpendicular component B_{perp} . The solid line is a theoretical fit (see Supplementary Note 3) showing $b^* = 0$ based on Hartree-Fock calculation of pseudospin anisotropy energy with finite-width corrections⁴ using sample parameters⁷ of effective mass $m^* = 0.0155$, Landé g factor $g = 54$, dielectric constant $\epsilon = 16.8$, and well width $d = 20$ nm. This fit does not consider the screening of Coulomb interactions and complex disorder effects, which may be responsible for the deviation of the fit from the data. Inset: b^*/k_B (where k_B is the Boltzmann constant) as a function of B_{perp} (or filling factor ν) at the tilt angle $\vartheta = 64.12^\circ$.



Supplementary Figure 11. **Activation energy Δ_{sw} for the spin-wave (SW)-mediated nuclear relaxation in neutral domain walls (DWs).** Δ_{sw} as a function of the magnetic field B (or filling factor ν) in phase II (dots) obtained by a fit to the data of $1/T_1$ versus T at different B (Fig. 2a, main text) using an Arrhenius law.



Supplementary Figure 12. **Comparison of the position of maximum $\Delta R_{\text{hys}}/R_{14,23}^{+B}$ and maximum $R_{14,23}^{+B}$ of the quantum Hall ferromagnet at filling factor $\nu = 2$.** Contour plot of the magnetic field B and the tilt angle θ as a function of $\Delta R_{\text{hys}}/R_{14,23}^{+B}$ is the same as that in Fig. 3a (see main text). Dots indicate the position of maximum $\Delta R_{\text{hys}}/R_{14,23}^{+B}$ (red) and maximum $R_{14,23}^{+B}$ (black), respectively. The solid line is a guide to the eye and the dashed line is calculated for the B and θ dependence of $\nu = 2$.



Supplementary Figure 13. **Nonlocal resistance of the quantum Hall ferromagnet at filling factor $\nu = 2$ for small currents.** Contour plot of the magnetic field B and the tilt angle θ as a function of $R_{14,23}^{+B}$ at a field-sweep rate of 1.7 mT/s, $I_{14} = 31.6$ nA, and $T = 1$ K. Red dots and the oval correspond to those shown in Fig. 2a (see main text). The solid line is a guide to the eye, and the dashed line is calculated for the B and θ dependence of $\nu = 2$.

Supplementary Table 1. Comparison of Zeeman energy and perturbative ratio α in GaAs 2DEGs and InSb 2DEGs (well width $d = 20 \text{ nm}$, $B = 13 \text{ T}$, magnetic length $l_B = 256 \text{ \AA}/\sqrt{B}$). Parameters are taken from Ref. 8 and from our experimental data.

	GaAs	InSb
effective g factor	-0.44	-54
Zeeman energy E_z (meV)	0.3	40
effective mass m^* (in units of m_0)	0.067	0.015
cyclotron energy (meV) $\hbar\omega_c = \hbar \frac{eB}{m^*}$	22.4	100
SOC coefficient γ (eV $\cdot \text{\AA}^3$)	27	500
SOC energy (meV) $\epsilon_{so} = \gamma \left(\frac{\pi}{d}\right)^2 / l_B$	0.1	1.7
perturbative ratio $\alpha = \epsilon_{so} / \hbar\omega_c$	0.0045	0.017

Supplementary References

1. McEuen, P. L., Szafer, A., Richter, C. A., Alphenaar, B. W., Jain, J. K., Stone, A. D., Wheeler, R. G. & Sacks, R. N. New resistivity for high-mobility quantum Hall conductors. *Phys. Rev. Lett.* **64**, 2062-2065 (1990).
2. van Son, P. C., de Vries, F. W. & Klapwijk, T. M. Nonequilibrium distribution of edge and bulk current in a quantum Hall conductor. *Phys. Rev. B* **43**, 6764-6767 (1991).
3. Jungwirth, T., Shulka, S. P., Shayegen, M & MacDonald, A. H. Magnetic anisotropy in quantum Hall ferromagnets. *Phys. Rev. Lett.* **81**, 2328-2331 (1998).
4. Jungwirth, T. & MacDonald, A. H. Pseudospin anisotropy classification of quantum Hall ferromagnets. *Phys. Rev. B* **63**, 035305 (2000).
5. Polyakov, D. G. & Shklovskii, B. I. Conductivity-peak broadening in the quantum Hall regime. *Phys. Rev. B* **15**, 11167-11174 (1993).
6. Polyakov, D. G. & Shklovskii, B. I. Variable range hopping as the mechanism of the conductivity peak broadening in the quantum Hall regime. *Phys. Rev. Lett.* **70**, 3796-3799 (1993).
7. Yang, K. F., Liu, H. W., Mishima, T. D., Santos, M. B., Nagase, K. & Hirayama, Y. Nonlinear magnetic field dependence of spin polarization in high-density two-dimensional electron systems. *New J. Phys.* **13**, 083010 (2011).
8. Winkler, R. *Spin-Orbit Coupling Effects in Two-Dimensional Electron and Hole Systems* (Springer, Berlin, 2003).